Numerical study on failure mechanism and acoustic emission characteristics of granite after thermal treatment

Yike Dang[1] · Zheng Yang[1] · Xiaoyu Liu[2] · Chunting Lu[3]

Abstract

To investigate the strength characteristics and failure mechanism of granite after thermal treatment are critical for geothermal energy storage and development. Acoustic emission (AE) is widely used to deduce the process of rock crack generation, development and penetration in laboratory tests, thus revealing the mechanism of rock failure. However, previous investigations have shown that laboratory tests cannot directly observe the interaction of thermal cracks and thermal stress, and more than 90% of AE tensile failure sources cannot be captured. This paper investigates the generation mechanism of thermal cracks and thermal stress distribution in thermally treated specimens using the discrete element method. After that, the evolution of AE failure sources is quantitatively analyzed by the moment tensor inversion results. The results showed that: (1) Thermal cracks destroy the internal structure of the specimen, thus weakening its mechanical properties. The number of thermal cracks increases with the temperature, further aggravating the damage to the mechanical properties of specimens; (2) as the temperature increases, the failure mode of the specimen changes from splitting failure to shear failure. Moment tensor inversion revealed that tensile failure dominated the final damage of samples. The shear and compaction failure sources increase with temperature, while tensile failure sources decrease; (3) the *b* value increased by 215% from 25 °C to 1000 °C. As the number of microcracks in a single AE event increases, the AE frequency decays exponentially, and most AE events have 1–5 microcracks.

Keywords Granite · Thermal damage · Acoustic emission · Failure mechanism · Moment tensors

1 Introduction

Geothermal energy has become a popular research topic because of its environmental friendliness, high efficiency and abundant reserves. Granite is the primary storage medium

✉ Zheng Yang
zyang@xjtu.edu.cn

Yike Dang
diryk0213@163.com

Xiaoyu Liu
xiaoyu-liu@xust.edu.cn

Chunting Lu
516750391@qq.com

[1] School of Human Settlements and Civil Engineering, Xi'an Jiaotong University, Xi'an 710049, China

[2] College of Sciences, Xi'an University of Science and Technology, Xi'an 710049, China

[3] China Construction Seventh Engineering Division.Corp.Ltd, Zhengzhou 450000, China

for geothermal energy reservoirs. During the drilling process, granite will continue to cool under the influence of room temperature working fluid, its mechanical properties will be weakened, and the fractures will be formed in the surrounding rock of the borehole. The fractures allow the circulation of fluids and cause continuous damage to the borehole. Furthermore, the safe implementation of underground disposal of high-level radioactive nuclear waste must consider the influence of temperature on the mechanical properties of the surrounding rock [1–5]. This is because the radioactive waste in a nuclear waste repository will emit heat during decomposition, and the accumulated heat can raise the surrounding temperature to 200–300 °C, causing thermal fracture in the surrounding rock [6]. The groundwater infiltration will further aggravate the surrounding rock's damage and result in nuclide emission, causing groundwater pollution. The surrounding rocks in the above two projects are in a high temperature-cooling environment, so it is crucial to study the strength characteristics and failure mechanism of rocks after thermal treatment to ensure the stability of

the surrounding rocks and the smooth development of the project.

Many studies have shown that temperature significantly impacts the physical and mechanical properties of rocks. After thermal treatment, the longitudinal velocity, density, peak strength and elastic modulus all decrease as temperature rises, but porosity and Poisson's ratio increase [2,4,7,8]. The change in physical parameters is closely related to water loss and structural damage caused by thermal reactions [9]. The mechanism of temperature effect on mechanical damage is as follows: due to the thermal expansion coefficient difference and the influence of thermal expansion anisotropy in minerals. The phenomenon of local thermal stress concentration between minerals is caused, leading the internal structure to change [10,11]. After exceeding a specific temperature, the stress acting on the boundary of minerals is greater than the strength limit of minerals. As new cracks are generated between or inside minerals, the primary cracks may fracture and expand [12]. Heat accumulated within the rock changed the structure of the relatively weak units. The higher the temperature, the greater the variation range of the internal structural system, resulting in more microcracks. Thermal stresses and thermal cracking caused by the temperature are the primary causes of mechanical property deterioration [13–15].

SEM (scanning electron microscopy) and AE (acoustic emission) monitoring [16,17] have been widely used to investigate the effect of thermal on the physical and mechanical properties of rocks. Nasseri et al. [18] applied the thin section image to analyze the Westerly granite after heating–cooling cycles; the microcracks and porosity increased with increasing temperature. The microcracks first appeared on the boundary of minerals and then propagate inside [19]. As the temperature increases, the crack expansion pattern changes from forward expansion of new cracks to continuous development of existing cracks [20]. AE can determine the thermal damage factor and the change in thermal cracking during heat treatment [21]. Some studies showed that the AE activity is concentrated around the peak strength region and microcracks induced at the edges are larger than inside [5]. Due to the limitation of equipment, there are still limitations in studying evolution process of microcracks. For instance, up to 90% of tensile failures cannot be monitored in experiments [22].

Numerical simulation can simulate complex experimental circumstances to supplement indoor experiments. The DEM (Discrete Element Method) aims to model a discontinuous medium. Accurate parameter calibration is the key factor to study the mechanical behavior of rock. The parameters are determined by the trial and error approach to make the simulation results match well with experimental observations. Parameter calibration has been discovered to be a time-consuming operation. In addition to DEM, the

extended rigid body spring network method (RBSN) [23,24], the extended finite element method (XFEM) [25,26], the phase field method [27,28], the meshfree method [29] and the peridynamic method [30,31] also can better simulate the brittle fracture of rock. The challenge of DEM in debugging parameters can be avoided with these simulation techniques. However, the DEM can model large deformation, crack propagation and object fracture since the particles can slip, rotate and separate. This advantage is not present in the research methods mentioned above.

Many scholars have investigated the mechanical behavior and fracture mechanism of rocks after heat treatment using DEM. Thermal stress and cracks inside the specimen increased with the temperature [32] and the microcracks propagate mainly through intergranular and intragranular [33]. The number of microcracks is directly related to the grain size, which decreases as the grain size increases [34]. The sudden value of thermal stress increases significantly with increasing temperature and produces considerable damage to the ends and edges of the rock [35]. The transverse thermal conductivity of the specimen varies nonlinearly with increasing axial stress due to the closure, sprouting and expansion of microcracks. The transverse thermal conductivity of the sample also varies significantly under different temperature treatments [36]. The specimen treated with high temperature exhibits a negative Poisson's ratio under low stress, the isolated massive clusters formed during the thermal treatment are the main reason for the negative Poisson's ratio [37]. The above research shows that DEM can well study the failure mechanism of rock under temperature.

AE in numerical simulation can analyze the microcrack evolution and explain the rock's failure process from the micro level. Hazzard and Young [38] introduced an approach for simulating AE in PFC and obtained the AE magnitude by a reasonable calculation method. After that, scholars have conducted quantitative investigations on the fracture characteristics of transversely isotropic rocks [39], the failure mechanism of rocks containing defects [40] and the mechanism of the effect of weak planes on hydraulic fracture propagation [41]. The results showed that AE numerical simulations based on moment tensor inversion can better describe crack sprouting, extension and interaction. The fracture information and moment magnitude of each AE event can be obtained.

AE test is widely used to deduce the process of rock crack generation, development and penetration in laboratory, thus revealing the mechanism of rock failure. However, AE technology is often limited in probe sensitivity, data storage and some AE events that cannot be monitored [22,42,43]. Furthermore, it is widely accepted that thermal stress is caused by the thermal expansion of minerals, resulting in thermally induced cracks. Because the change in thermal stress distribution and microcrack property under different thermal

loading paths is difficult to obtain in laboratory tests, there are few relevant studies. Thus, this paper investigates the failure mechanism and AE characteristics of granite after thermal treatment at the microscopic level using DEM. The distribution of the thermal stress, the evolution of AE characteristics and the failure mechanism of the granite after loading are examined. This research has significant implications for the advancement of underground engineering in a high-temperature environment.

2 Modeling approach

2.1 Thermal calculations in DEM

In DEM thermal simulation, particles are modeled as heat reservoirs and their contacts as heat flow paths. After setting appropriate thermal parameters and boundaries, thermal simulation can calculate temperature and heat flux distribution in heat conduction. Thermal modeling follows the heat conduction equation and Fourier's law. For a single reservoir, the heat conduction equation is [44]:

$$-\sum_{p=1}^{N} Q^{(p)} + Q_v = mC_v \frac{\partial T}{\partial t} \tag{1}$$

where $Q^{(p)}$ is the power, Q_v is the heat source intensity, m is the thermal mass, C_v is the specific heat, T is the temperature.

Each pipe is regarded as a one-dimensional line of length L, the power (Q) in a pipe is given by:

$$Q = -\frac{\Delta T}{\eta L} \tag{2}$$

where Q is the power in a pipe, ΔT is the temperature difference between the two reservoirs on each end of the pipe, η the thermal resistance.

In practice, the thermal conductivity (k) can be measured, and for isotropic materials, there is a relationship between thermal conductivity and thermal resistance: [10]:

$$\eta = \frac{1}{2k} \left(\frac{1-n}{\sum_{N_b} V^{(b)}} \right) \sum_{N_p} l^{(p)} \tag{3}$$

where N_p is the active thermal pipes of balls, n is the porosity, $V^{(b)}$ is the volume of the particle, N_b is the numbers of the particles, $l^{(p)}$ is the length of each pipe, k is thermal conductivity.

As particles thermally expand, the material will generate thermal strain. Assuming that the change of temperature is

ΔT, the particle radius changes as follows:

$$\Delta r = \alpha r \Delta T \tag{4}$$

where α represents the thermal expansion coefficient; r, Δr represent the particle radius and the change value, respectively.

If a linear parallel bond is present at the mechanical contact associated with a thermal contact, we assumed that temperature affects only the normal component of the bonding force. When parallel bonding contacts a heat pipe and the material expand isotropically, the normal component of the bonding force changes as [44]:

$$\Delta \overline{F}_n = -\overline{k}_n A(\alpha L_1 \Delta T) \tag{5}$$

where $\Delta \overline{F}_n$ is the bond normal force, $\overline{k}_n$ is the bond normal stiffness, A is the area of the bond cross section and L_1 is the bond length.

2.2 Moment tensor algorithm in DEM

In this study, the moment tensor approach was used to quantify the mechanism of the seismic source and calculate the AE magnitude. The moment tensor and its components were calculated by integrating the microcracks at each time step following the bond fracture based on the change in contact position and contact force: [39]

$$M_{ij} = \sum_{S} \Delta F_i L_j \tag{6}$$

The M_{ij} is the scalar seismic moment, ΔF_i is the ith component of the contact force change, L_j is the jth component of the distance between the contact point and the AE event centroid and the sum is performed in the range of the S surface, enclosing the AE event. The moment tensor can be calculated in real-time using this method, but it will consume much memory. Hence, the moment tensor with the largest scalar moment was chosen as the moment tensor of the AE event, and the scalar moment (M_0) can be obtained by Eq. 7 [45]:

$$M_0 = \left(\frac{\sum_{j=1}^{3} M_j^2}{2} \right)^{1/2} \tag{7}$$

The M_j is the jth eigenvalue of the moment tensor matrix.

The AE's moment magnitude (M_w) indicates the event's influence range and the energy released by each event, it can be calculated using Eq. 8 [46]:

$$M_w = \frac{2}{3} \log M_0 - 6 \tag{8}$$
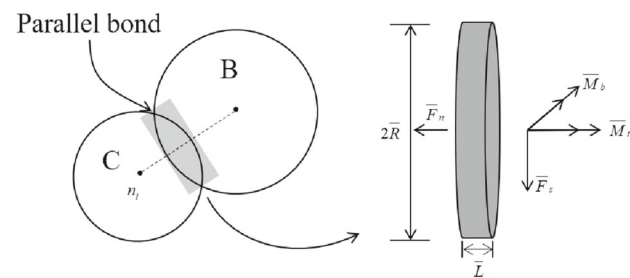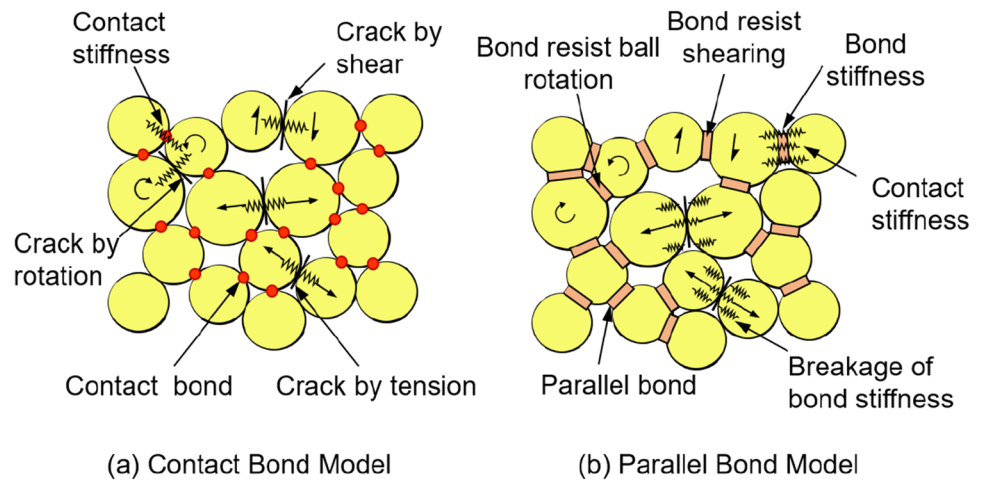
Fig. 1 Two bond models in DEM [51]

Contact stiffness · Crack by shear · Bond resist ball rotation · Bond resist shearing · Bond stiffness · Contact stiffness · Crack by rotation · Contact bond · Crack by tension · Parallel bond · Breakage of bond stiffness

(a) Contact Bond Model   (b) Parallel Bond Model

Fig. 2 Decomposition of force and moment in parallel bond model [53]

Parallel bond · B · C · n_i · $2\overline{R}$ · $\overline{F}_n$ · $\overline{M}_b$ · $\overline{M}_t$ · $\overline{F}_s$ · $\overline{L}$

Fig. 3 Mechanisms of microcrack generation in DEM [35]

Particle A · Particle B · Particle C · Particle D · Crack shear · Crack tension

Feigner and Young quantize the failure mechanism of AE events using the ratio of isotropic to deviatoric part of the moment tensor [47,48], R can be expressed as:

$$R = \frac{tr(M) \times 100}{|tr(M) + \sum\limits_{i=1}^{3} m_i*|} \tag{9}$$

where $tr(M)$ is the moment tensor trace, m_i* is the deviatoric eigenvalue.

The ratio (R) ranges between -100 and 100. When R is larger than 30, less than -30, or between -30 and 30, the AE event is described as tensile failure, compaction failure, or shear failure, respectively [40].

3 Numerical modeling and micro-parameters calibration

The DEM was proposed by Cundall [49] for solving rock mechanics problems and then applied to soils by Cundall and Strack [50]. PFC2D simulates the movement and interaction of stressed assemblies of rigid circular particles using the DEM. It allows finite displacements, rotations and complete separation of discrete bodies and automatically recognizes new contacts. The motion of a single rigid particle is deter-
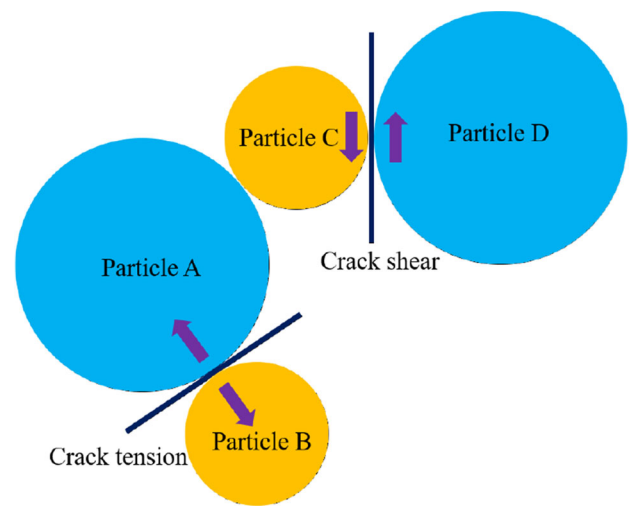
mined by the resultant force and moment vectors acting upon it and can be described in terms of the translational motion of a point in the particle and the rotational motion of the particle.

There are two major types of bonding models available: the parallel bond model and the contact bond model (Fig. 1). The difference is that the former can transmit both forces and moments and mostly used for rock simulation. The parallel bond model simulates the physical behavior of a cement-like material connecting two adjacent particles (B and C in Fig. 2). The relative motion of particles will generate forces and moments at the cementation and act on particles at both ends of the bond. The contact area between particles can be regarded as a disk. The initial values of both the parallel bond force $\overline{F}$ and moment $\overline{M}$ are zero after parallel bond formation.

$\overline{F}$ can be decomposed into normal $\overline{F}_n$ and shear components $\overline{F}_s$. $\overline{M}$ is resolved into a twisting $\overline{M}_t$ and bending moment $\overline{M}_b$. After that, the normal $\overline{\sigma}$ and shear stress $\overline{\tau}$ on

Table 1 Physical parameters of the numerical model

Model parameters	Value
Size, $W \times H$ (mm)	50×100
Minimum particle size, $R_{\min}$ (mm)	0.4
Particle size ratio, v	1.66
Porosity, p	0.16
Particle number, N_b	20290
Particle density, ρ (kg/m^3)	2750

Table 3 Thermal expansion coefficients of minerals [56]

Thermal expansion coefficient α, 10^{-6}/°C	Value
Quartz	24.3
Plagioclase	14.1
K-feldspar	8.7
Biotite	3.0
Amphibole	23.8

the parallel bond can be described as: [52]

$$\begin{cases} \bar{\sigma} = \dfrac{\bar{F}_n}{A} + \bar{\beta}\dfrac{\|\bar{M}_b\|\overline{R}}{\overline{I}} \\[4mm] \bar{\tau} = \dfrac{\|\bar{F}_s\|}{A} + \begin{cases} 0, & 2D \\ \bar{\beta}\dfrac{\|\bar{M}_t\|\overline{R}}{\overline{J}}, & 3D \end{cases} \end{cases} \quad (10)$$

where A is the parallel bond cross-sectional area, $\overline{R}$ is the bonding radius, $\overline{J}$ is the polar moment of inertia of the parallel bond cross-sectional area, $\overline{I}$ is the moment of inertia of the parallel bond cross-sectional area, $\overline{\beta}$ is moment contribution factor, with $\overline{\beta} \in [0, 1]$.

If the force acting on a bond exceeds the tensile or shear strength, the bond will be broken. The force, moment and stiffness on the bond will all vanish simultaneously, and a tensile or shear crack is formed (Fig. 3). The bonding between particles A and B is subject to the radial force and then slides in the radial direction. When the radial force exceeds the tensile strength, the bonding will be breaking, thus generating tensile cracks. When the shear force between particles C and D exceeds the shear strength, the bond will be ruptured, resulting in a shear crack.

3.1 Model building

The numerical model used to study the granite has the same size as the report by Liu et al. [54]. The particle sizes of the model were distribution ranging from 0.4 to 0.664 mm.

To determine the reasonable filling of the model, the initial porosity was set to 0.16. According to previous studies [55], the parallel bond model was chosen as the bond model between particles. The model parameters of granite are listed in Table 1.

In this study, the granite is composed of quartz, plagioclase, K-feldspar, biotite and amphibole. Diopside and magnetite, which have a negligible proportion since their effect on mechanical and thermal response is limited [10]. The minerals and contents of the sample are listed in Table 2. To accurately reflect the thermal behavior of the minerals, it is necessary to assign thermal expansion coefficients to the different minerals. The thermal expansion coefficients are summarized in Table 3. The specific heat of all particles is set to 1015 J/kg·°C.

The cellular automata simulation is used to create a numerical model with equal proportions of minerals based on the mineral composition in Table 2 [57]. The purpose of the cellular automaton approach is to create a "cluster" model that reflects the uneven shape of the mineral. The numerical model is presented in Fig. 4. The establishment process is as follows: If the mineral types in n are included in the sample, first set the properties of all particles as matrix minerals and the proportion of other minerals as random seed generation. The proportion of each mineral in the mineral seed automatically determines the mineral type [58]. The probability that the particle ith in contact with a certain mineral particle is the same type is:

Table 2 The mineral composition in the granite sample

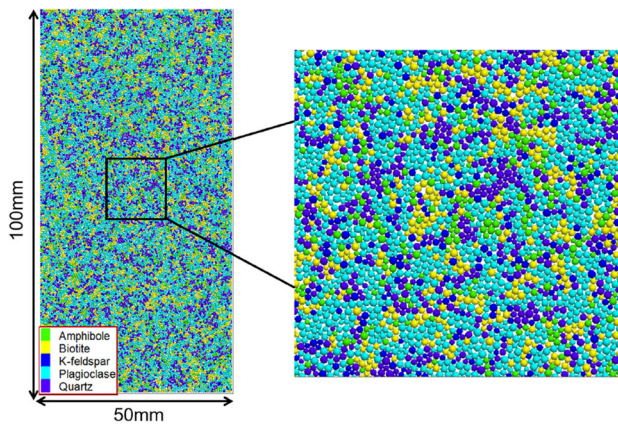| Minerals	Mineral composition in experimental/%	Mineral composition in numerical/%
Quartz	17	17
Plagioclase	37	45
K-feldspar	8	8
Biotite	18	18
Amphibole	12	12
Diopside	4	0
Magnetite	4	0

Fig. 4 Numerical model containing multiple minerals

Table 4 The micro-parameters for the numerical model

Parameters	Values
Effective modulus of the particle, E_c (GPa)	25.5
Stiffness ratio of the particle, k_n/k_s	1.2
Effective modulus of the parallel bond, E_b (GPa)	25.5
Stiffness ratio of the parallel bond, k_{nb}/k_{sb}	1.2
Friction coefficient, f	0.5
Tensile strength, σ_c/MPa	52
Friction angle, $\varphi/°$	50
Cohesion, c/MPa	68
Moment contribution factor, β	0

$$p_i = (V_n - V_c)/V_n \tag{11}$$

V_n is the final target area of the nth mineral, and V_c is the current existing area when the nth mineral is generated. When the mineral type and ratio are specified, the program will repeatedly calculate and guide every mineral to reach its proportion.

To avoid the thermal shock on the effect of thermal cracking [59], the sample was heated uniformly with 10 °C for every timestep. The model will calculate until the ratio of the maximum unbalanced force to the average force of all particles was less than 0.01. Previous studies have shown that the phase of quartz will change from α to β at 573 °C. When the temperature increased to 573 °C, the radius of quartz is expanded by 1.0046 times, and the radius will be shrunk by 0.9954 times when the temperature decreased to 573 °C [34]. This method is used to simulate the phase transition of quartz.

3.2 Calibration of micro-parameters

The micro-parameters of the granite model are determined by the 'trial and error' method. When the mechanical param-

eters, such as peak strength and elastic modulus are closed to the experimental, it is proven that micro-parameters can accurately reflect the physical and mechanical properties of granite. The 'trial and error' approach has been widely introduced in previous studies [60], hence, it is not repeated here.

The parallel bonding model, which considers the contact between particles as a point contact, has been proven to overestimate the specimen's tensile strength. In this paper, the problem of high tensile to compressive ratios is solved by modifying the failure criterion of the parallel bond model (By modifying the moment contribution factor to zero) (Eq. 10) [61]. Table 4 lists the micro-parameters used in this paper. The numerical and experiment results for granite at different temperature treatments after loading are compared in Fig. 5. The numerical results agree with the experimental data in the stress–strain curve, peak strength and elastic modulus.

When the temperature is lower than 400 °C, the peak strength is almost constant with increasing temperature, whereas it rapidly decreased when the temperature exceeds 400 °C (Fig. 5c). The elastic modulus obtained by numerical is larger than the experimental, ranging between 200 °C to 1000 °C (Fig. 5d). These differences are caused by the chemical reactions of the minerals and melting at high temperature conditions, which cannot be simulated by software. Thus, as the temperature exceeds 200 °C, the peak strain obtained by the numerical is less than that of the experiment, resulting in a greater elastic modulus (Fig. 5d).

According to some investigations [51,55], spherical particles underestimate the sample's peak dependency, resulting in a high ratio of tensile strength to compressive strength, which may produce an error between numerical results and the experiment. Reference [62] provides methods to avoid these errors.

4 Results and discussion

4.1 Analysis of thermal damage

4.1.1 Distribution of microcracks inside samples after thermal treatment

The microcracks distribution after different temperature treatments is shown in Fig. 6. The black and red lines represent tensile and shear cracks, respectively. The mechanical characteristics of the specimens remained unchanged at 100 °C, only thermal expansion take place, and no microcracks are observed. However, temperature variations will impact the internal structure of the specimen [11].

At 200 °C, the microcracks begin to appear in the specimen. All microcracks are tensile cracks that are randomly
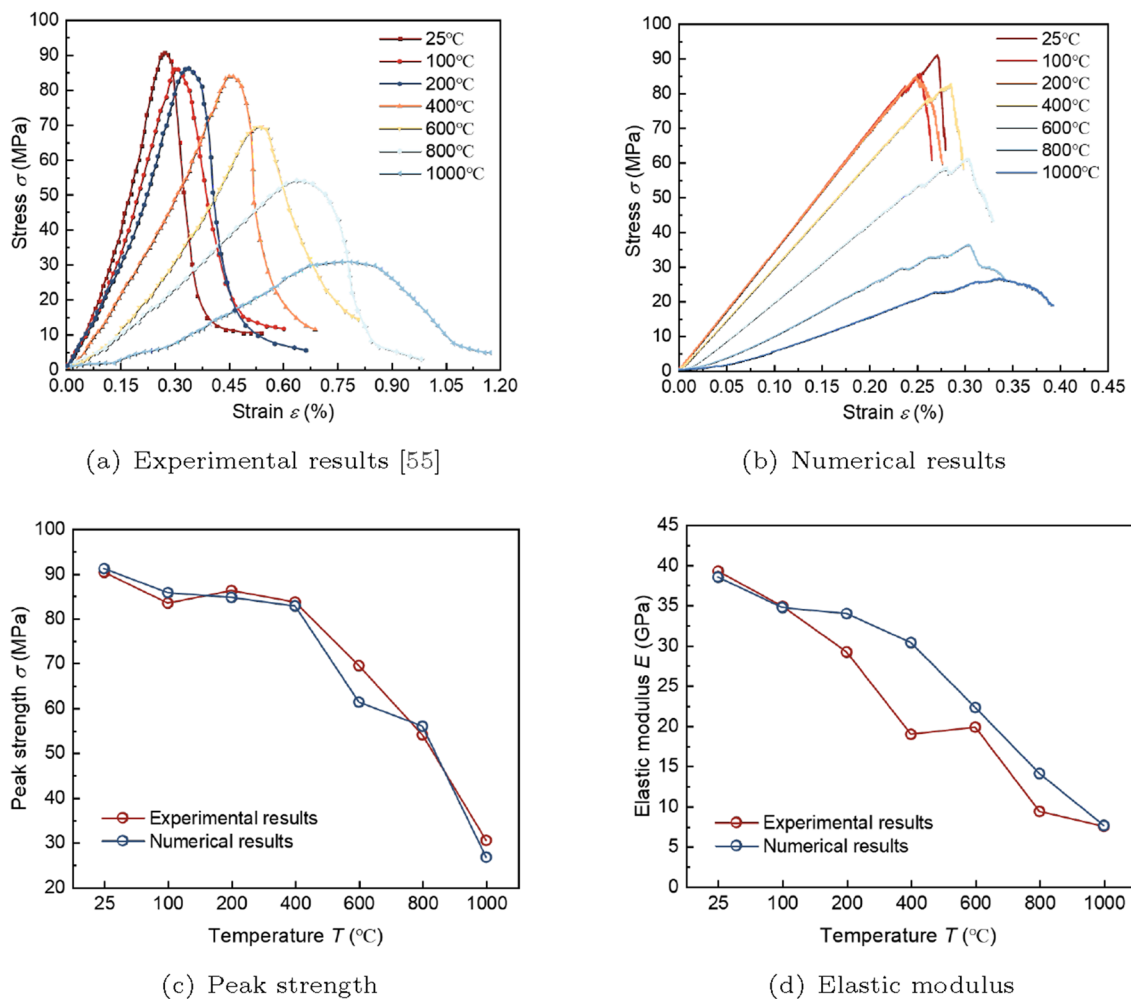
(a) Experimental results [55]

(b) Numerical results

(c) Peak strength

(d) Elastic modulus

Fig. 5 Comparison of experimental and numerical stress–strain curves, peak strength and elastic modulus after loading test

dispersed and do not aggregate. At 400 °C, the microcracks coalesce partially and even connect to form large fractures, with the total microcracks reaching 5431. Thermal stress caused massive thermal damage from 600 °C to 1000 °C, and more microcracks are produced, which may further grow into macro fractures. The formation of fractures aggravates the specimen's internal structure damage degree. The temperature has a positive correlation with the number of microcracks. However, the growth rate of microcracks is inconsistent throughout temperature ranges, with a maximum between 400 °C and 600 °C.

The number of intragranular and intergranular cracks are plotted in Fig. 7. Most of the microcracks are formed between grains with different thermal expansion coefficients. The specimen produced only 59 microcracks at 200 °C. A significant number of microcracks begin to appear when 400 °C is reached, with the number exceeding 3000.

Due to the phase transition of quartz, from 400 °C to 600 °C, the rate of crack formation reaches its peak. Compared to

400 °C, the number of cracks has increased by 126% at 600 °C. More than 62 % of microcracks are intergranular, occurring mostly at the interface of minerals with different thermal expansion coefficients. Plagioclase predominated among the four minerals, accounting for more than 19% of the intragranular microcracks. Although plagioclase does not have the greatest thermal expansion coefficient, but it has a high proportion in the specimen, followed by amphibole and quartz with a large thermal expansion coefficient. K-feldspar and biotite have the smallest microcracks because their thermal expansion coefficient and proportion are the lowest.

The microcracks grow linearly from 600 °C to 1000 °C, but the growth rate decreases by 39% compared to 600 °C. The number of intergranular cracks reduces by 3% at 1000 °C and the proportionate distribution of intragranular cracks matches the temperature in 600 °C.

Fig. 6 The distribution of microcracks inside the specimens after different temperature treatments. The black and red lines are tensile and shear cracks, respectively. (Color figure online)
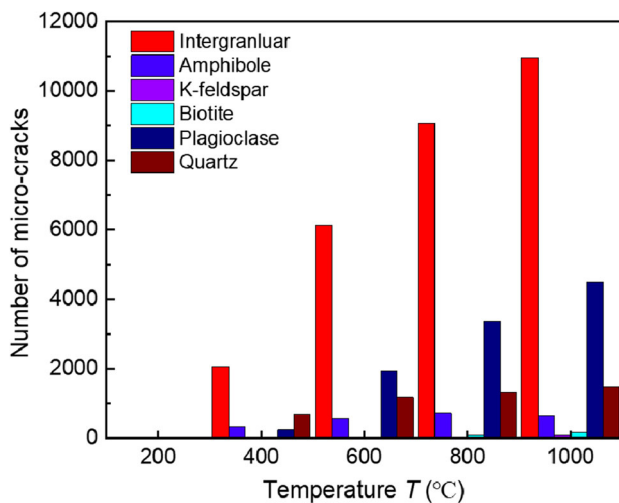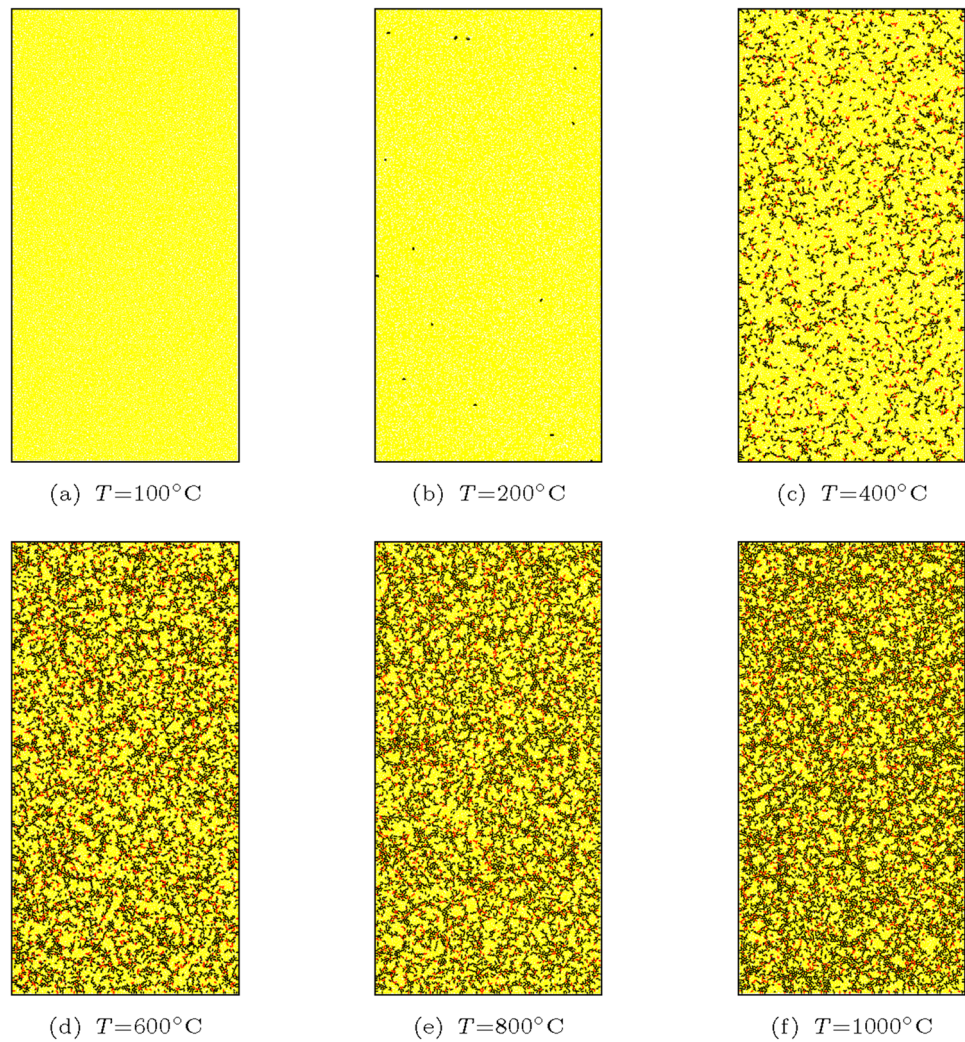

(a) $T=100°$C

(b) $T=200°$C

(c) $T=400°$C

(d) $T=600°$C

(e) $T=800°$C

(f) $T=1000°$C

Fig. 7 The number of microcracks inside the specimens after different temperature treatments

4.1.2 Distribution of thermal stress inside samples after thermal treatment

The local tensile and compressive stress concentrations will be formed inside the sample at high temperatures. Since the minerals are spread out randomly in the model, the tensile and compressive stresses differ in value and degree. The stress field are recorded using measurement circles, and it can further analyze the influence of thermal damage on the mechanical properties of samples. The radius of the measurement circle is 2.5 mm, and a total of 200 are created. It should be noted that by default, the tensile stress is positive, and the compressive stress is negative.

The evolution of thermal stress is shown in Fig. 8. The thermal stress of the sample is mainly tensile stress, with a maximum value of 0.02 MPa at 100 °C, and a portion of the compressive stress area is formed, with a maximum value of 0.01 MPa. At 200 °C, two concentrated tensile stress zones are formed, which are composed of the plagioclase, quartz and amphibole. The plagioclase's deformation is smaller than
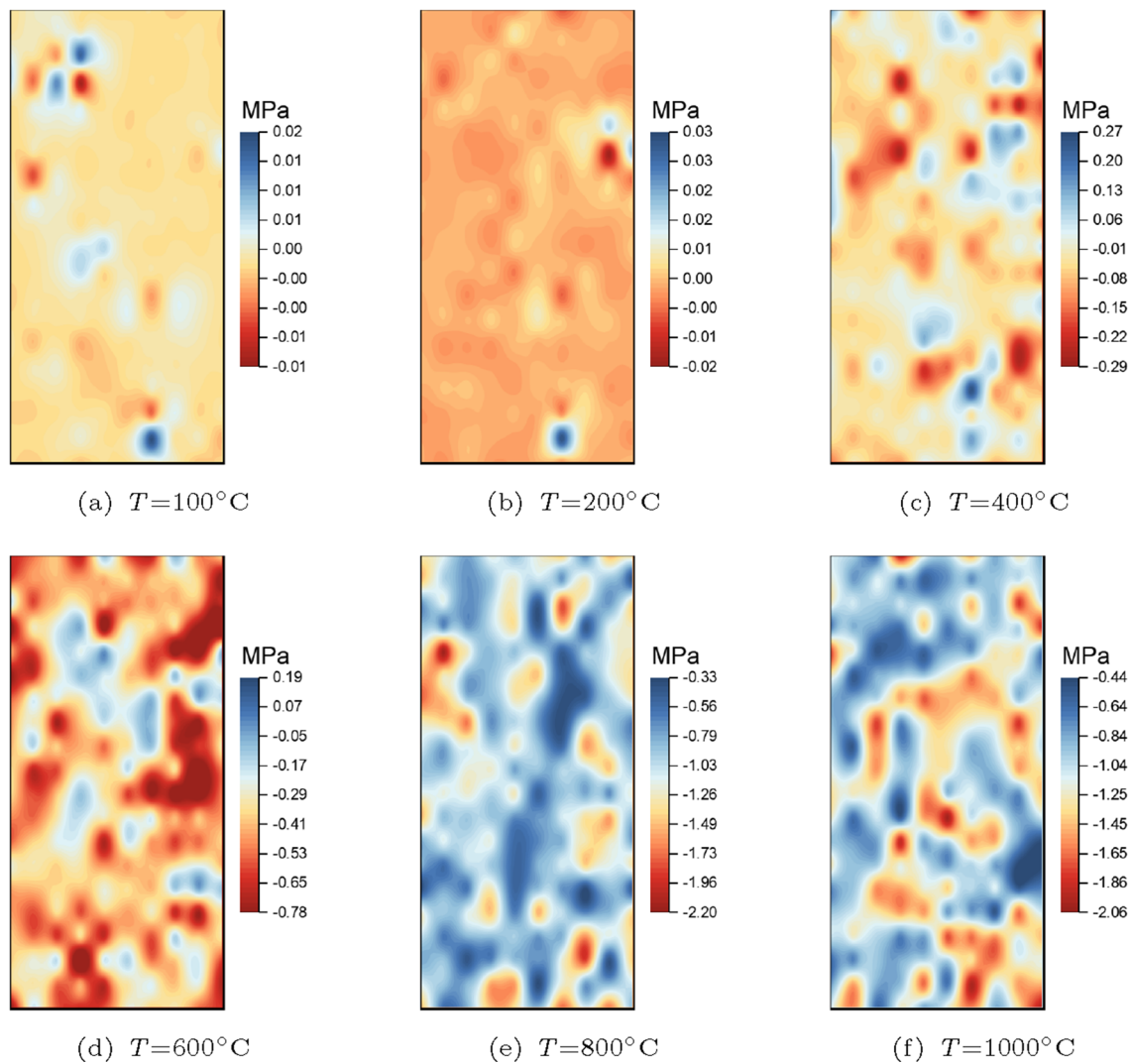
Fig. 8 Thermal stress distribution of the specimens after different temperature treatments, the negative and positive values represent compressive and tensile stresses, respectively

quartz and amphibole due to its lower thermal expansion coefficient. Hence, local tensile stress is generated in this area.

The tensile and compressive stress concentration regions both increased rapidly at 400 °C, but the compressive stress concentration regions are dominant, with the maximum stress value of 0.29 MPa. Due to the minerals squeeze each other frequently, the thermal stress is all compressive stress at 800 °C. At 1000 °C, the maximum compressive stress value exceeded 2MPa. This value is increased about seven times compared to the 400 °C. The compressive stress concentration area increased significantly, and there appeared in almost every region, causing the greatest degree of structural damage to the specimen.

4.1.3 Distribution of local thermal stress and microcracks after thermal treatment

The evolution of local contact force chains and microcracks under different treatment is plotted in Fig. 9. (The black line represents the contact force, while the thickness of the line reflects the contact force value.) The number of contact stress concentration areas and the maximum value increase with temperature. The generation of thermally induced cracks significantly affects the stress distribution between particles, there is an interaction between both. As can be seen in Fig. 9, there are a larger number of microcracks distributed in the stress concentration region.

There are only a few contact force concentration areas below 400 °C and they are not connected to each other. Above 400 °C, microcracking develops rapidly and its proportion increases with increasing temperature. The contact
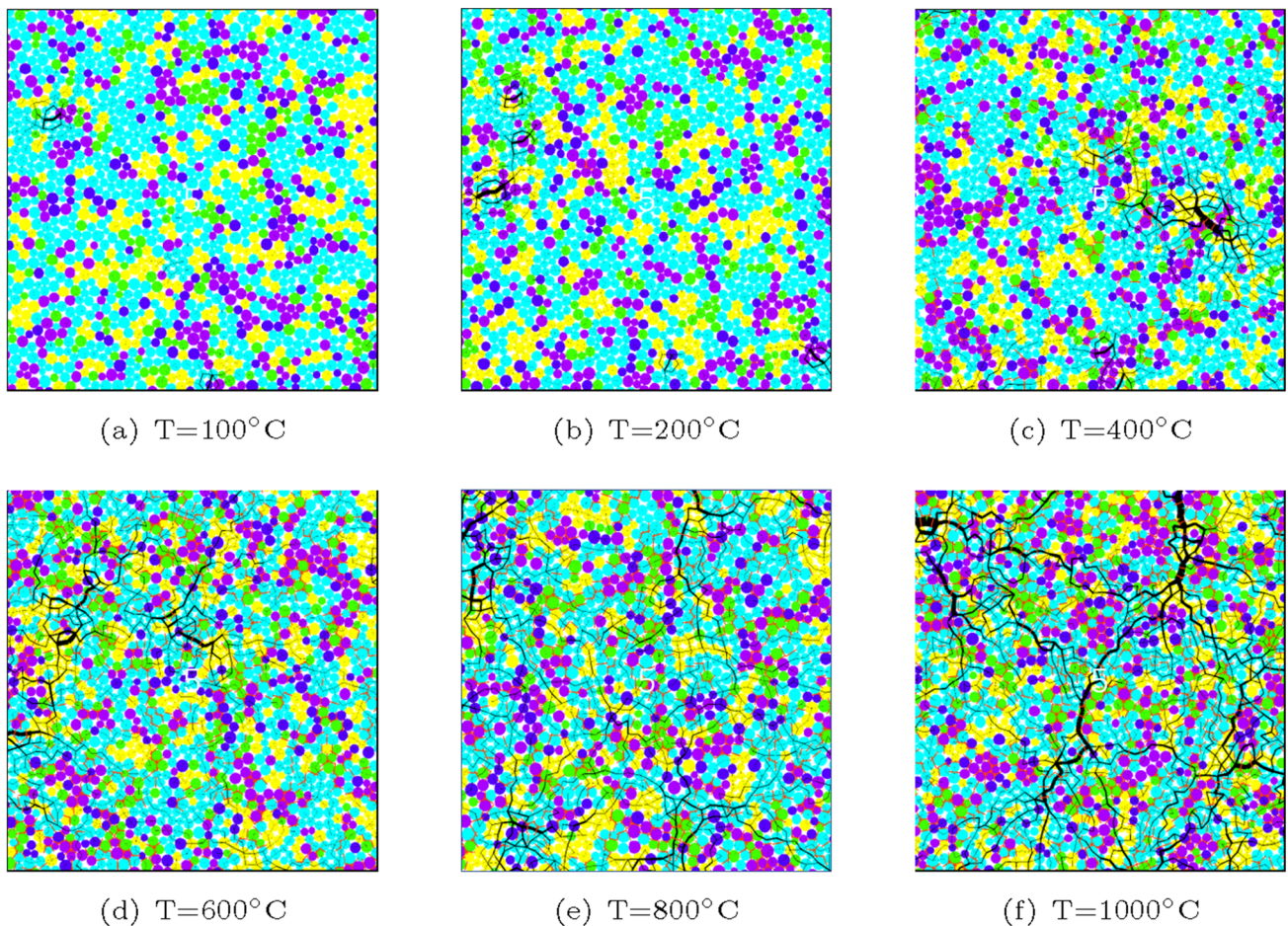
Fig. 9 Local display of contact forces and microcracks inside the specimens after different temperature treatments. The thickness of the black line represents the magnitude of the contact force, the red line are the microcracks. (Color figure online)

force developed further within minerals with a lower thermal expansion coefficient, and it promotes the connection of different contact force concentration areas. The contact forces in turn promotes the formation of microcracks. The above research reveals that the damage degree of rock's internal structure by temperature is connected to the mineral thermal expansion coefficient, mineral content and mineral strength limit.

Figure 10 shows the optical micrograph of thermally induced cracks in granite after high temperature treatment. There are no obvious thermally induced cracks to be observed at 200 °C. At 400 °C, intergranular cracks form mainly between feldspar and feldspar, quartz and feldspar. Meanwhile, no transgranular cracks are generated. At 600 °C, the phase change of quartz causes multiple intergranular cracks at the quartz–feldspar interface and transgranular cracks within the quartz. At 800 °C, microcracks promote each other and progressively develop macrofractures, significantly increasing crack width. The numerical evolution of crack types is similar to the experiment.

In summary, when rocks are heated, the mineral particles within will not deform freely in accordance with their inherent thermal expansion coefficients. Therefore, mineral particles are constrained, the mineral with large deformation is compressed and the small deformation is stretched. Thus, the thermal caused stress concentration zone formed in the rock. A large proportion of the thermal stress concentration area is a crucial factor that causes the mechanical characteristics of the sample to deteriorate.

4.2 Influence of temperature on the failure mechanism of granite

4.2.1 Spatial distribution of AE events after loading test

The AE distribution of the samples at different thermal treatments after loading is shown in Fig. 11. The cyan, blue and red circles represent the tensile, compaction and shear failure, the radius represents the AE magnitude. The magnitude indicates the fracture strength of the AE events. The number

Fig. 10 Thermally induced cracks observed in the laboratory test [63]. "bc" means "boundary crack," "tc" means "transgranular crack." Q, F and B represent quartz, feldspar and biotite, respectively

(a) T=200°C

(b) T=400°C

(c) T=600°C

(d) T=800°C
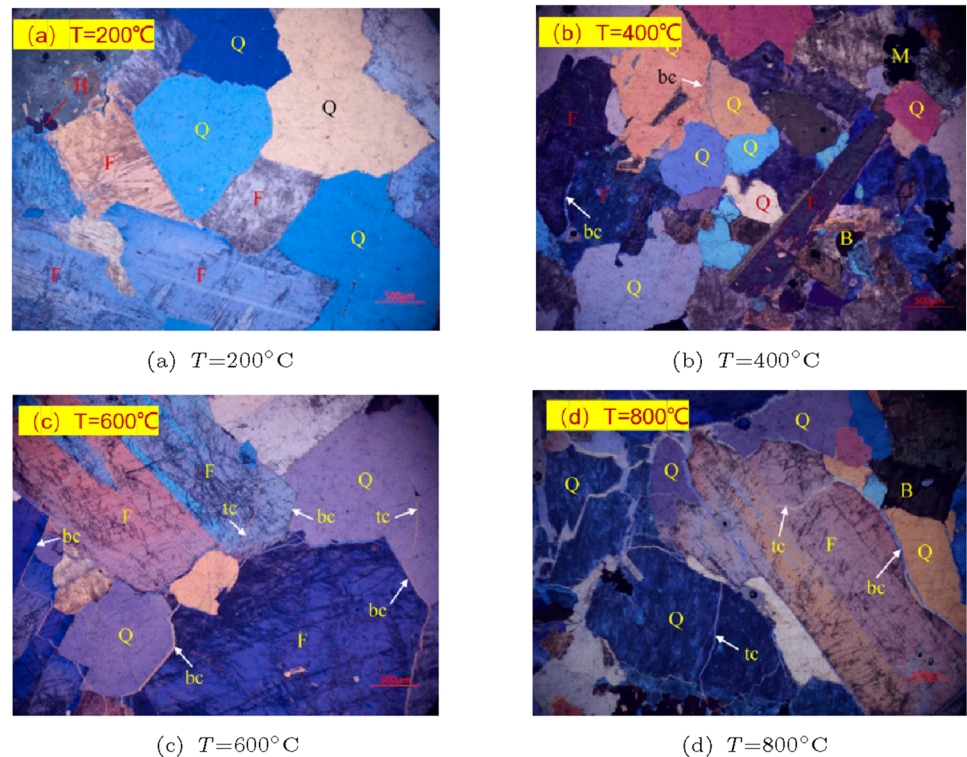
of AE events and their magnitude both decrease as temperature increases.

The distribution of the AE events in high temperature samples (T = 600 °C, 800 °C, 1000 °C) are more scattered than low temperature (T = 25 °C, 100 °C, 200 °C, 400 °C) and the AE magnitudes are relatively low, this is due to the significant structural damage within these samples. The failure source of AE events in all samples is dominated by tensile.

For the low temperature conditions (below 400 °C), the obvious fracture failure can be observed, the AE events are concentrated in the macrofracture zone. In areas outside the fracture zone, the AE magnitudes are relatively small. (The radius of the circle is smaller than the circle of the fracture zone.) These cracks failed to penetrate to form large fractures, and they released less energy during the damage process and did not stimulate the formation of more microcracks in the surrounding area.

From 600 °C to 1000 °C, the range of bond failure is enormous, compared to the samples treated at temperatures below 400 °C, there is no apparent macroscopic fracture zone. At this point, most AE events are composed of individual microcracks. The thermal damage causes a significant increase in defects and porosity within the specimen, leading to the disorderly development of microcracks. Thus, the AE events are scattered in the specimens. Furthermore, the failure mode of the sample inclined to plastic failure as temperature increased, indicating that the effect of temperature leads to an intensification of the rock plastic failure trend.

Many investigations show that the sample's failure mode shifts from splitting to shear as the temperature increase [64–66], which is consistent with the findings in this research.

The proportion of AE failure sources after loading is shown in Fig. 12. The tensile failures first increased, then decreased and peaked at 600°C, accounting for 81% of the total events. The shear and compaction failure source first reduced and then increased with the temperature. Tensile failures, independent of temperature, dominated the AE's failure type of all samples.

The polar coordinate histogram of microcracks distribution after loading is shown in Fig. 13. The length of each bin represents the number of microcracks within the angle range defined by the bin. The orientation of the microcracks is mainly parallel to the direction of the vertical stress, since the bond in the loading direction is prone to failure under load, which leads to the microcracks forming and expanding easily in the vertical loading direction [67]. Below 400 °C, the microcracks form primarily in the 90 ° direction. With the increase in temperature, the distribution of the crack is dispersed from 90 ° to 180 ° and 0 °. This result indicates that in the vertical loading direction, the tendency of the sample expansion increases, and the bearing capacity decreases.

4.2.2 Evolution of AE events at 100 °C and 800 °C under different stress levels

Analyzing AE event distribution and failure sources during loading allows for a quantitative investigation of the failure
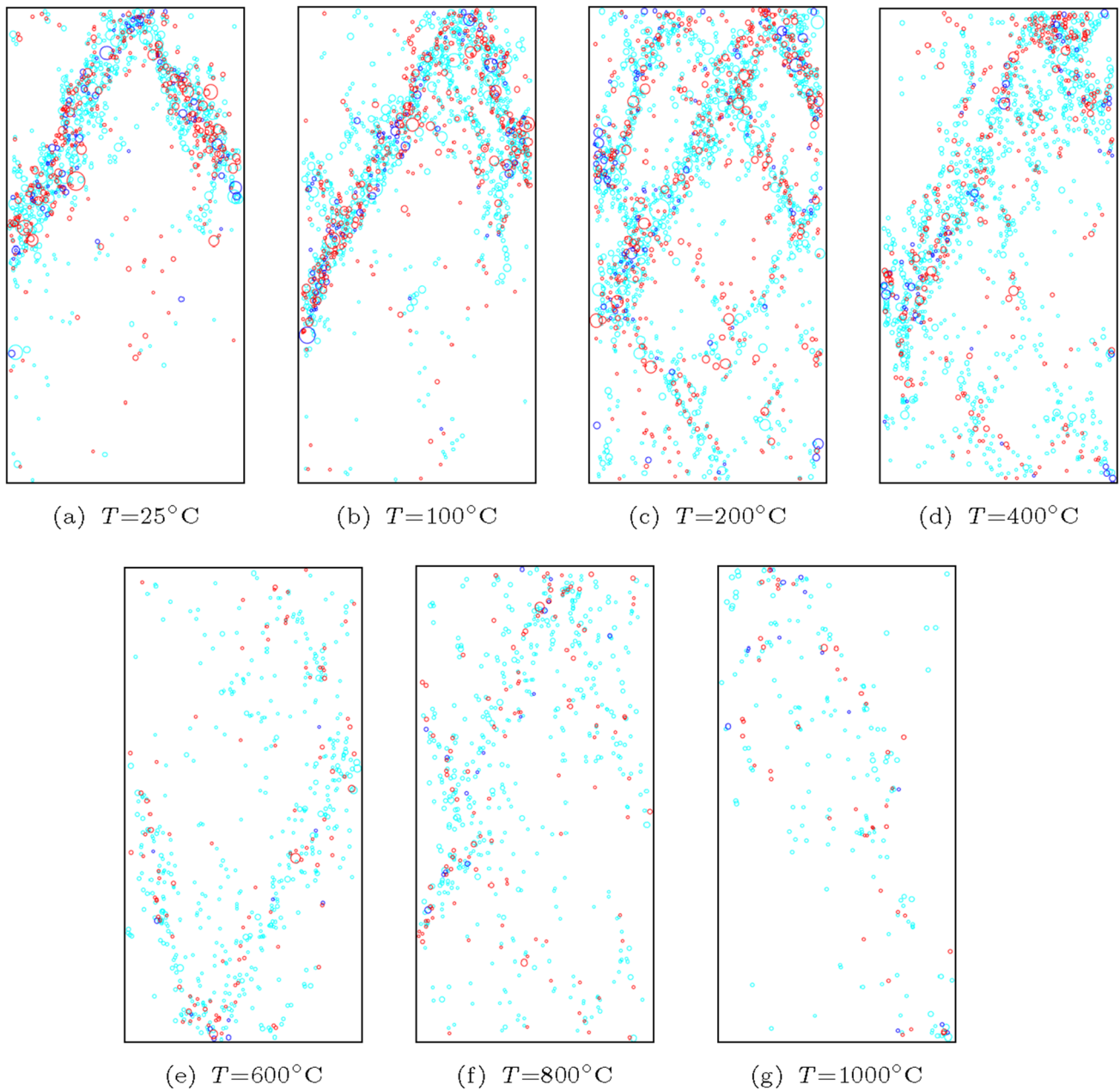
Fig. 11 The distribution of AE events of thermally treated specimens after loading. Each circle represents an AE event and the radius represents the AE magnitude; the tensile, compaction and shear failures are indicated by cyan, blue and red circles. (Color figure online)

mechanism of thermally treated specimens. The stress–strain curve and AE magnitude of the 100 °C treated after loading are shown in Fig. 14. The six points (a, b, c, d, e, f) on the stress–strain curve represent different stress levels, corresponding to the 80% before the peak (Pre-peak 80%), 90% before the peak (Pre-peak 90%), at the peak, 90% after the peak (Post-peak 90%), 80% after the peak (Post-peak 80%), 70% after the peak (Post-peak 70%), respectively. In the Pre-peak stage, most AE events have magnitudes ranging from −5.0 to 5.6 (with a maximum value of −5.0) and have fewer AE events. After the peak, while magnitudes are primarily

between −4.5 and 5.8, the number of AE events increased rapidly, resulting in many high magnitude occurrences (with a maximum magnitude value −4.5).

The proportion of AE source type at different stress levels is summarized in Fig. 15. Before the peak point, the proportion of tensile failure increased with increasing stress, while the proportion of shear and compaction failure gradually decreased. However, the evolution trend of the AE failure source is the opposite after the peak.

The specimen failure produced many microcracks from the peak point to the post-peak 90%. The macrotensile fail-
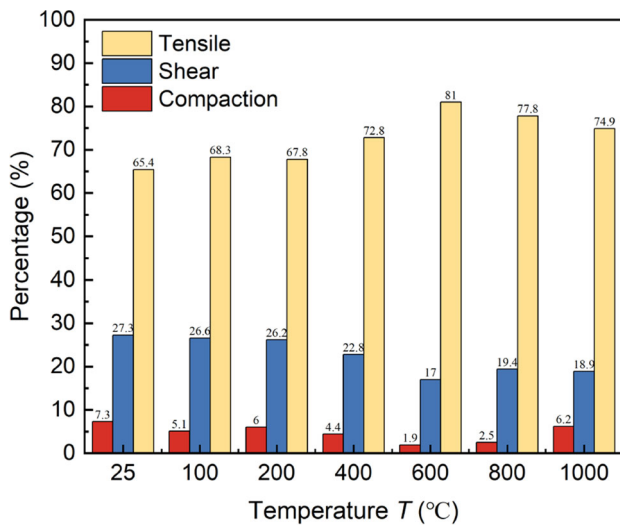
Fig. 12 The proportion of AE failure sources for different temperature treated specimens after loading. (The yellow, blue and red color for tensile, shear and compaction failures, respectively). (Color figure online)

ure gradually develops from post-peak 90% to post-peak 80% to cause particle instability around the fracture. The rate of microcrack growth remained rapid and the tensile failure source increased by 6.53% in this stage. In the stage between post-peak 80% and post-peak 70%, the microcracks are fully developed, and the increasing rate slows down. The slip dislocation and friction from macrofractures are the main causes of small magnitude events (minimum magnitude value −5.8), and the proportion of shear and compaction failures also increased.

Figure 16 shows the distribution of AE events corresponding to each point in Fig. 14. In the pre-peak stage, a few AE events are scattered in the specimen and caused by the closure and friction of microcracks. These AE events, which are mostly composed of a single crack, indicate that there is no structural damage in the sample. The number and magnitude of AE events increased dramatically from peak to post-peak 90%, and several events overlapped. The occurrence of these AE events can be seen as a precursor of sample failure.

Some independent microcracks are randomly generated and then generated AE events at the peak point (point c) and Pre-peak stages (at points a and b). In these stages, most AE events are composed of a series of independent microcracks, and only a few AE events contain multiple. As the load increased, the number of AE events erupted before and after the peak point, much energy is consumed during the microcrack penetration and macrofracture formation. Thus, a series of high magnitude AE events are generated (with a maximum magnitude value −4.5).

The microcracks merged to form macrofractures and propagated from post-peak 90% to post-peak 80%. The degree of particle friction and slip on both sides of the fracture surface increased, and the number of AE events grow explosively. The old and new cracks connect, which eventually causes the rock failure. The magnitude of AE events has increased, indicating that frequent interaction between cracks and accompanied by the release of a large amount of energy. The AE events in the macrofracture zone are primarily of moderate intensity (magnitude −5.2 to −4.7), and the specimen eventually destroys along this path.

Figure 17 shows the stress–strain curve and AE magnitude of the 800 °C treated sample after loading. The AE events developed earlier in the 800 °C treated specimens than in the 100 °C, with magnitudes ranging from −5.6 to 5.1 and remaining stable throughout the loading period. The high temperature severely damages the internal structure of the specimen, and even with a minor external load, the sample can form microcracks, which in turn generate AE events, causing the events to occur early. During the compression, it is not easy to accumulate energy in the sample, so no high magnitude events are produced.

Figure 18 shows the distribution of AE failure sources at different stress levels. The tensile failure sources increase while shear failures decrease at the pre-peak stage, and the post-peak trends are the opposite. Tensile failure sources are reduced by 5.35% from Pre-peak 90% to Post-peak 70%, but shear and compaction failure sources increased by 4.29% and 1.07%, respectively. Tensile failure sources, on the other hand, constantly dominated.

Thermal damage increases specimen flaws at 800 °C, which can easily connect between microcracks under load and generate macro fractures. The 100 °C heat hardly changed the internal structure of the sample; the particles are always under compression before the damage. There is frequent inter-sliding and compression activity between particles, and the microcracks are interconnected but not penetrating. Thus, the 800 °C treated specimens had a lower proportion of shear and compaction failure sources than 100 °C.

Figure 19 shows the distribution of AE events corresponding to the six different stress levels in Fig. 17. Overall, the AE magnitude in the 800 °C treated specimens are smaller than in the 100 °C (Reflected in the radius of the circle). This also reflects the thermal damage to the mechanical characteristics of the specimen from the side. There are no large magnitude AE events formed before and after the peak, which is also different from the 100 °C thermally treated specimen.

The AE events are randomly distributed in each part of the specimen, and there is essentially no interaction. All AE events consist of a single microcrack, and the magnitude dis-
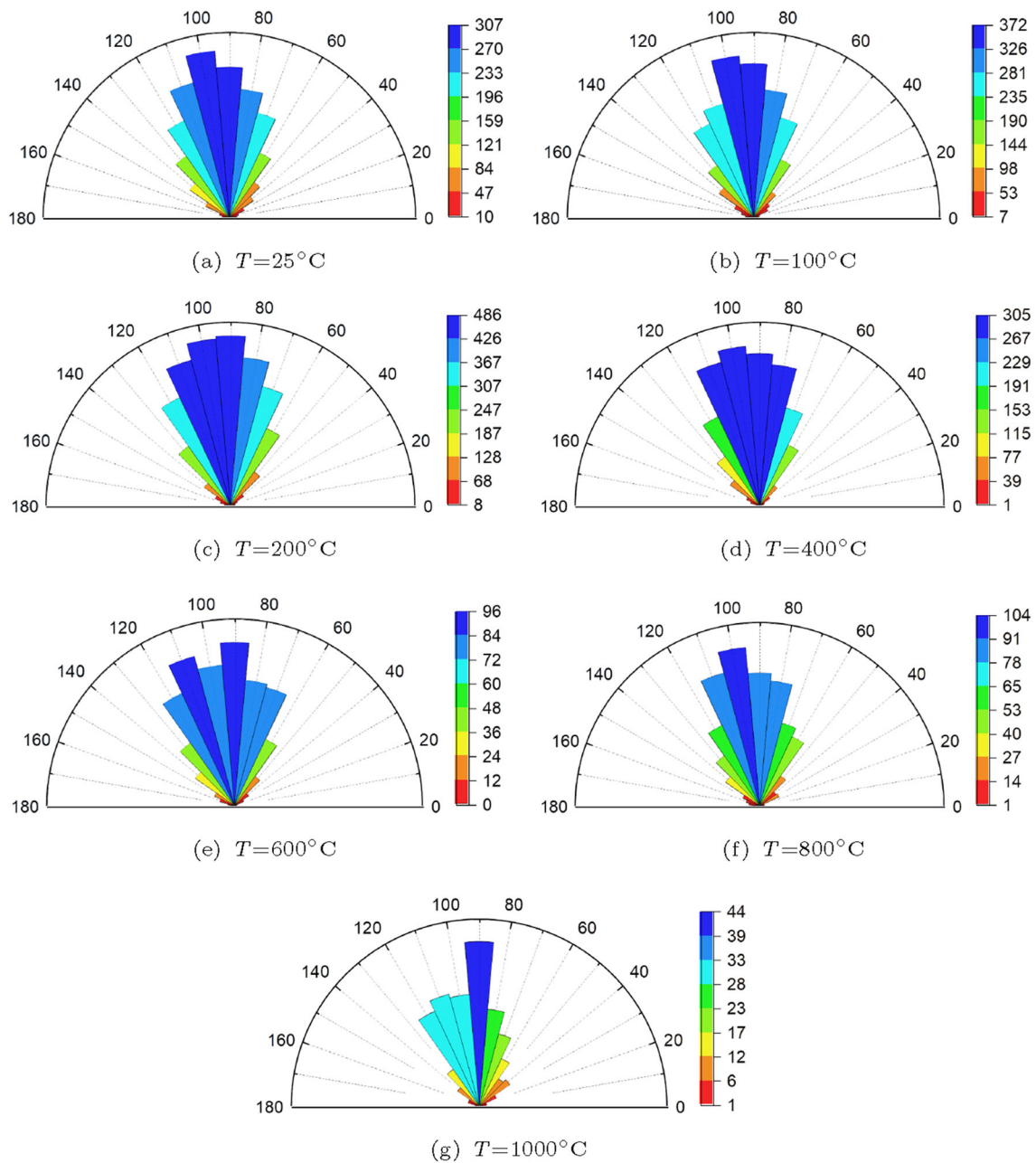
Fig. 13 The orientation distribution of microcracks in the specimen after loading. The color of the bin represents the number of microcracks, with blue and red representing the maximum and minimum values, respectively. (Color figure online)

tribution between ranging from -5.1 to 5.6. When the load reaches the post-peak 90%, the cracks display a clustering and nucleation trend. However, unlike at 100 °C, the microcracks do not have a clear direction of expansion and continue to be formed randomly in the areas that have the most severe thermal damage. At post-peak 70%, there is no macrofracture formed, and the microcracks are always without a fixed direction of expansion. The high temperature-treated specimens are more prone to microcracking under external forces and have a more similar AE magnitude distribution throughout the loading process.

4.2.3 Effect of temperature on the frequency and magnitude of AE events

A bonded broken may represent an AE event, and the rupture of multiple bonds may also constitute an AE event. However, the magnitudes that constitute the two types of AE events mentioned above are different. The number of microcracks contained in a single AE event is proportional to its magnitude. Investigating the relationship between the number of AE events and magnitude will contribute to a deeper understanding of the AE characteristics of the samples.
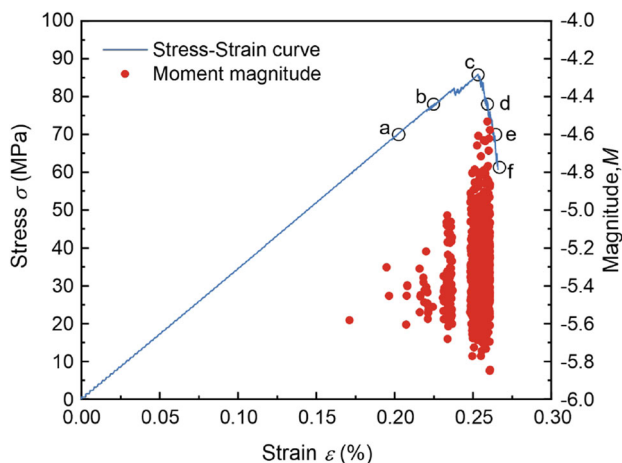
Fig. 14 The stress–strain curve of specimen after treatment at 100 °C. Each solid circle represents an AE event and the right axis shows its magnitude; the six points (a, b, c, d, e and f) represent 80% before the peak (68.70 MPa), 90% before the peak (77.29 MPa), peak (85.88 MPa), 90% after the peak (77.29 MPa) and 80% after the peak (68.70 MPa) on the curve are captured to investigate the microcrack initiation and propagation.
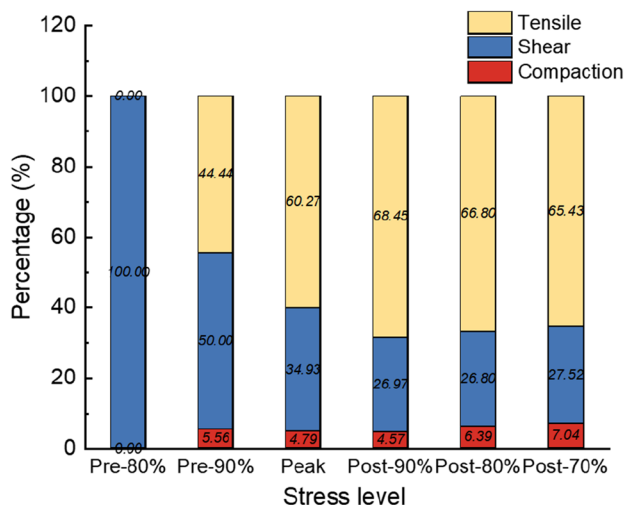

Fig. 15 The proportion of AE failure sources for specimens after 100 °C treatment at different stress levels. (The yellow, blue, and red color for tensile, shear and compaction failures, respectively). (Color figure online)

Fig. 16 The distribution of AE events at different stress levels in specimen treated at 100 °C, corresponding to six points (a, b, c, d, e and f) in Fig. 14. (Each circle represents an AE event and the radius represents the AE magnitude)

(a) Pre-Peak 80%

(b) Pre-Peak 90%

(c) Peak

(d) Post-Peak 90%

(e) Post-Peak 80%

(f) Post-Peak 70%
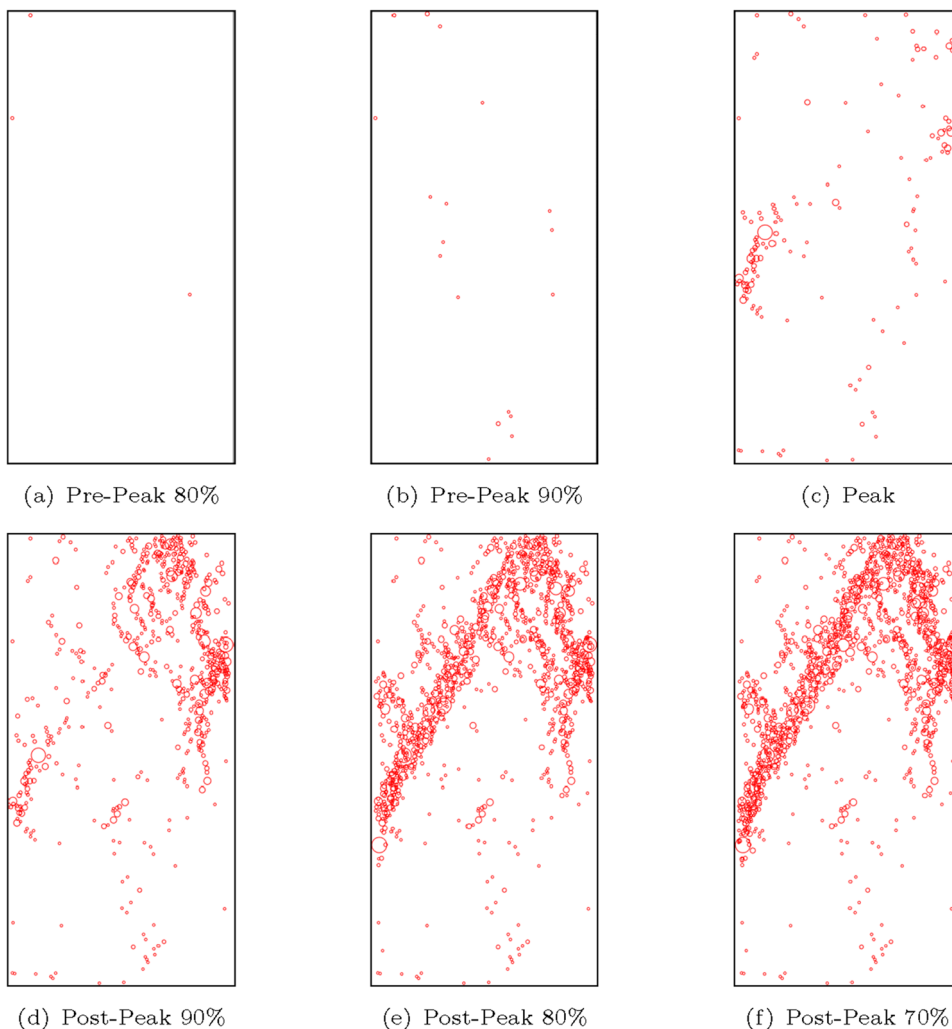
The relationship between the cumulative number of AE events, AE frequency and AE magnitude is shown in Fig. 20. The AE magnitude is mainly distributed between −5.5 and 5.2, the frequency of AE events gradually decreases when the magnitude is greater or less than this range. The temperatures have obvious effect on the frequency–magnitude distribution. For example, at the 25 °C (Fig. 20a), the frequencies of magnitude between −5.5 and 5.2 is 766, accounting for 61% of total AE events. The proportions of frequencies of magnitudes between −5.5 and 5.2 corresponding to the temperatures of 100–1000 °C are 68%, 76%, 77%, 79%, 88% and 91%, respectively. This proportion increases as temperature increases, indicating that the magnitude range of AE events decreases as temperature increases.

Some researchers have demonstrated that AE events' cumulative number and magnitude follow a power-law distribution [68], the AE magnitude and frequency follow the normal distribution. In 1941, Gutenberg and Richter put forward the famous G-R formula between earthquake magnitude and frequency, it can be used to study the AE magnitude:

$$Log N = a - bM \tag{12}$$

where N is the cumulative number of AE events with magnitudes greater than N and a, b are constants. This relation is widely used to investigate the relationship between b values and crack growth. The constant a represents the average level of activity in the local area studied. b value is an essential parameter in AE research, it represents the frequency of small magnitude events compared to large magnitude of the rock failure process. (The b value is inversely proportional to the number of large magnitude events. The large magnitude indicates that the energy released by the AE event is large and the more microcracks it contains.) The change of b value is one of the crucial precursors of rock failure.

The b value can be calculated by fitting the number of AE events with magnitudes ranging from −5.75 to −5.0 in Fig. 20. The relationship between the b value and temperatures is shown in Fig. 21. The b value changes slightly from 25 °C to 200 °C and increases by about 0.41. It increased by about 91% in an approximately linear trend from 400 °C to 1000 °C, with a maximum value of 5.96. The high temperature causes significant structural damage to the specimen and increases internal defects, coupled with the phase change of quartz at 573 °C. The microcracks are easily generated when subjected to external load. The AE events are mainly composed of a single microcrack, and their intensity varies little, so the b values tend to increase linearly.

Figure 22 shows the relationship between the AE magnitude and the cumulative number of events at different temperatures after loading. The maximum magnitude of AE events is observed to decrease with increasing temperature, with a maximum magnitude value of −4.45 at 25
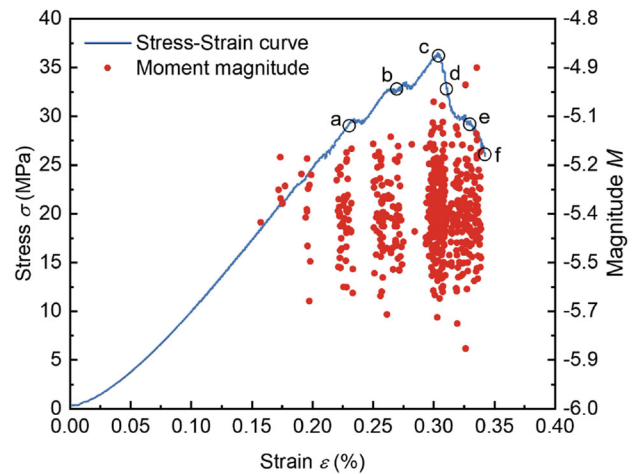
Fig. 17 The stress–strain curve of specimen after treatment at 800 °C. Each solid circle represents an AE event and the right axis shows its magnitude; the six points (a, b, c, d, e and f) represent 80% before the peak (29.24 MPa), 90% before the peak (32.90 MPa), peak (36.55 MPa), 90% after the peak (32.90 MPa) and 80% after the peak (29.24 MPa) on the curve are captured to investigate the microcrack initiation and propagation
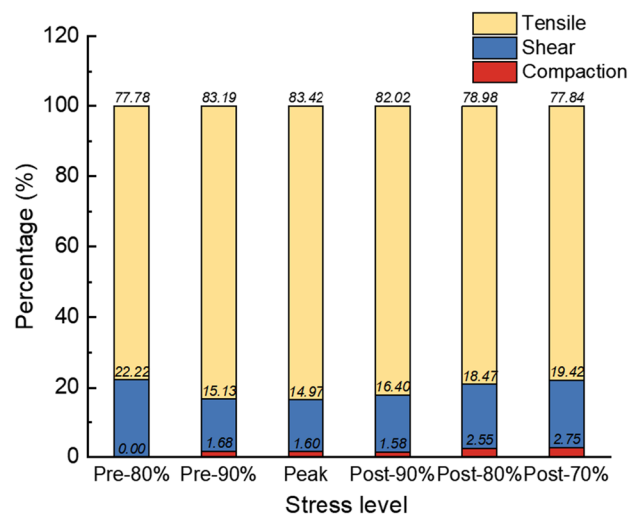

Fig. 18 The proportion of AE failure sources for specimens after 800 °C treatment at different stress levels. (The yellow, blue and red color for tensile, shear and compaction failures, respectively). (Color figure online)

°C and −5.15 at 1000 °C, a decrease of 15.7%. However, the minimum magnitude values do not change significantly. Furthermore, the cumulative number of AE events did not vary markedly over the range 25–400 °C. The number of AE events decreased by 59% from 400 °C to 800 °C and 61% from 800 °C to 1000 °C. The number and magnitude of AE events both decrease dramatically with increasing temperature.

Falls [69] performed a uniaxial compression test on Lac du Bonnet granite at room temperature, and the result indicated the b value distribution ranging from 1.3 to 2.3. The b

Fig. 19 The distribution of AE events at different stress levels in specimen treated at 800 °C, corresponding to six points (a, b, c, d, e and f) in Fig. 17. (Each circle represents an AE event and the radius represents the AE magnitude)

(a) Pre-Peak 80%   (b) Pre-Peak 90%   (c) Peak

(d) Post-Peak 90%   (e) Post-Peak 80%   (f) Post-Peak 70%
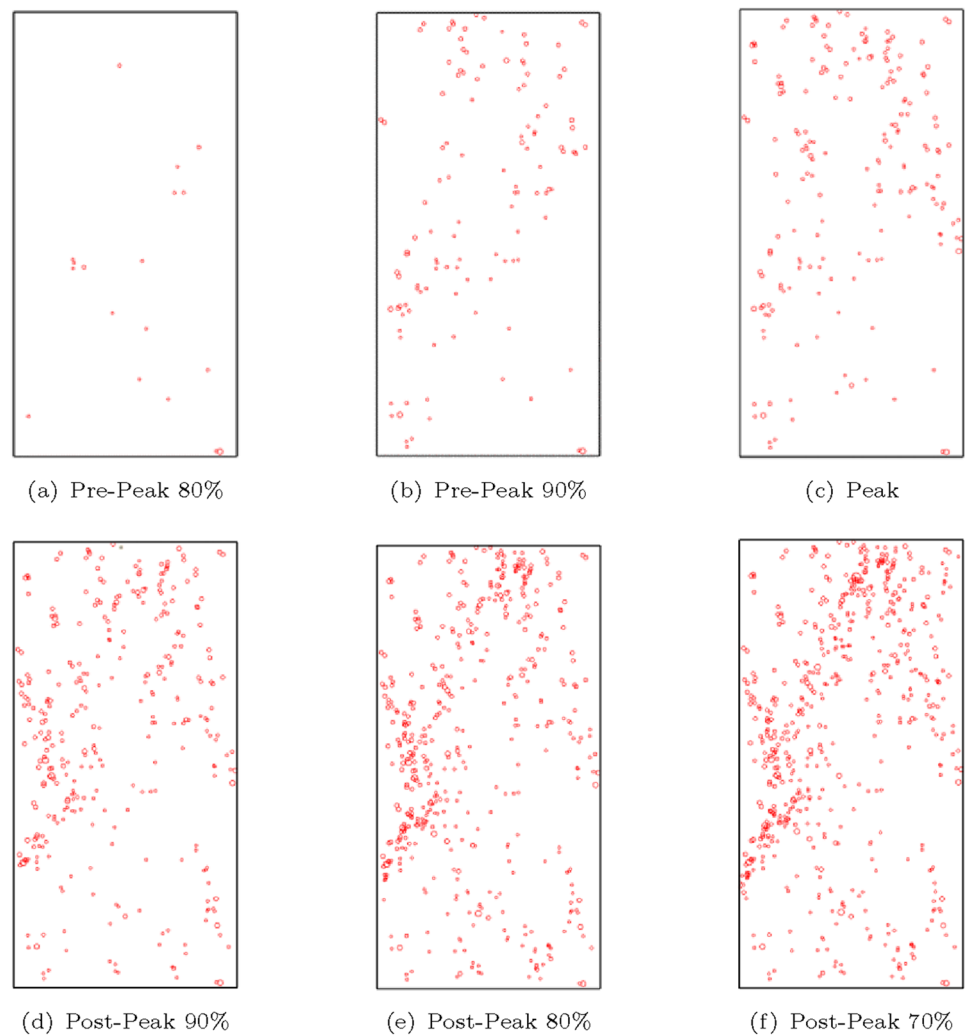
value obtained by numerical is distributed between 1.89 and 2.3 at 25–200 °C, which is consistent with the experimental results. This also demonstrates that numerical simulations can accurately reflect the AE information during rock failure and can obtain small magnitude events that are not captured in the laboratory [70]. Furthermore, some studies have shown that up to 90% of tensile failure source cannot be captured in the laboratory. In contrast, AE simulations allow us to examine all the damage mechanisms involved in the failure of the rock and provide a new approach to the deeper investigation of rock damage mechanisms [22].

The relationship between the AE frequency and the crack number is shown in Fig. 23. The AE frequency decays exponentially as the number of microcracks in a single AE event increase. There are 774 AE events composed of a single microcrack at 25 °C, accounting for 66.11% of all events. The number of AE events with 1–5 microcracks accounts for 97% of the total events. The proportion of AE events containing a single microcrack is 67.4%, 67.1%, 76.9%, 95.3%, 86.4% and 92.1% in the range of 100–1000 °C, this

indicates that most AE events consist of a single microcrack.

From 25 °C to 1000 °C, the number of AE events containing 6–10 microcracks is 43, 35, 39, 13, 3, 0 and 0, exhibiting a decreasing trend with increasing temperature, accounting for 0.04%, 0.03%, 0.02%, 0.01%, 0.005%, 0% and 0% of the total events, respectively. These findings confirmed the previous conclusions about the b value: the number of AE events with multiple microcracks decreased significantly with increasing temperature, while the number of AE events with a single microcrack increased.

5 Conclusion

In this paper, the mechanism of microcrack generation in granite after thermal treatment is studied using DEM, and thermal stress development is analyzed. After that, the evolution of AE failure sources is examined using the moment tensor inversion results. The numerical results agree well

Fig. 20 The cumulative of AE event, AE frequency and AE magnitudes at different temperatures of the specimen; the frequency and magnitude of AE events follows a normal distribution; b value is obtained by fitting the slope of the line with magnitude at $-5.75 \sim -5.0$ with 1.89, 2.27, 2.30, 3.12, 4.97, 5.10, 5.96, respectively, corresponding to temperatures of 25 °C, 100 °C, 200 °C, 400 °C, 600 °C, 800 °C and 1000 °C, respectively
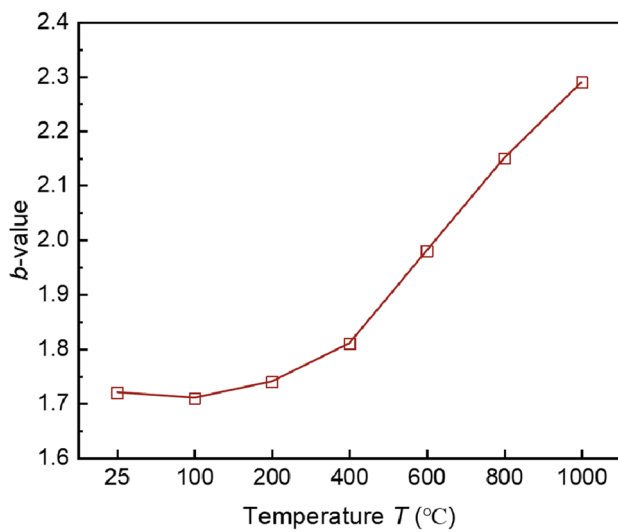

(a) $T=25°C$

(b) $T=100°C$

(c) $T=200°C$

(d) $T=400°C$

(e) $T=600°C$

(f) $T=800°C$

(g) $T=1000°C$
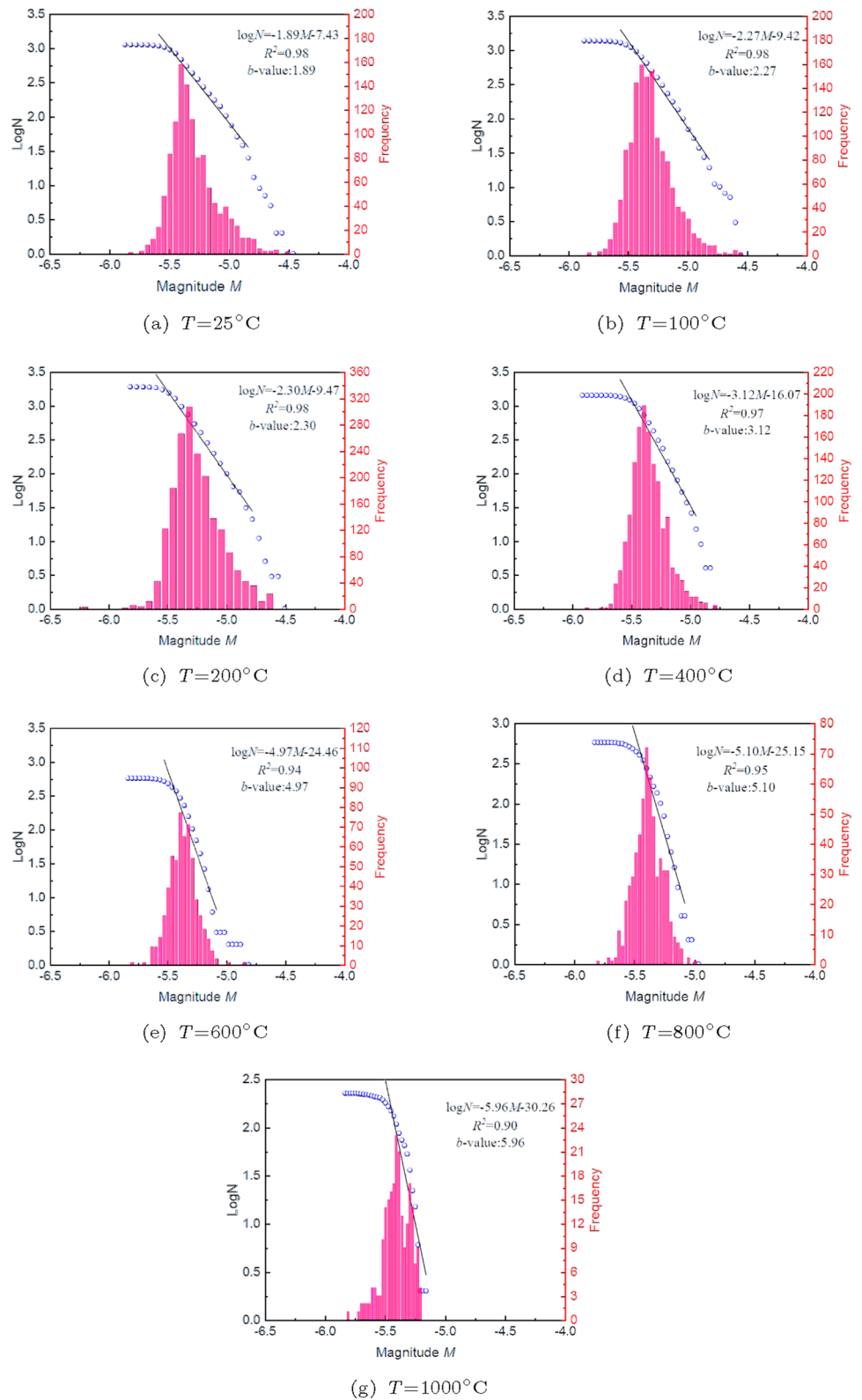
Fig. 21 The relationship between temperatures and *b* value; the *b* value increases linearly above 400 °C
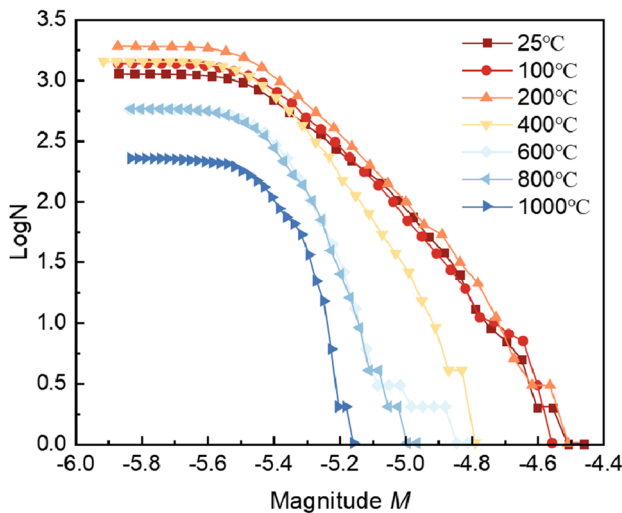

Fig. 22 The relationship between the AE frequency and magnitude at different temperatures; the AE maximum magnitude value decreases as temperature increases

with the experiment, and main conclusions of this study are as follows:

(1) There is a relationship between the microcracks and temperature, and the process of evolution can be divided into three stages. Within 200 °C, there are no microcracks. The growth rate of microcracks reaches a peak between 400 °C and 600 °C due to the phase transition of quartz. Thermal stress causes thermal damage and more microcracks inside the sample above 600 °C, aggravating the deterioration of the mechanical properties. The primary form of thermally induced cracks is intergranular cracks.

(2) Tensile failure increases and then decreases with temperature, peaking at 600 °C and accounting for 81% of total events. Shear and compaction failure show a temperature-dependent trend of decreasing and then increasing. The AE events in the damage process of all specimens are dominated by tensile failure sources and independent of temperature.

(3) The frequency and magnitude of AE events have a normal distribution, while the cumulative number and magnitude of AE events have a power-law distribution. Temperature has a clear effect on the magnitude distribution of thermally treated samples, the AE maximum magnitude value decreases as temperature increases.

(4) The *b* value increases with temperature, indicating that the number of AE events with multiple microcracks decreases with increasing temperature. As the number of microcracks in a single AE event increases, the AE frequency decays exponentially, and most AE events have 1–5 microcracks.

Fig. 23 The AE frequency decays exponentially as the number of microcracks in an AE event increase; most of the AE events contain 1–5 microcracks; the number of AE events with multiple microcracks decreased with increasing temperature
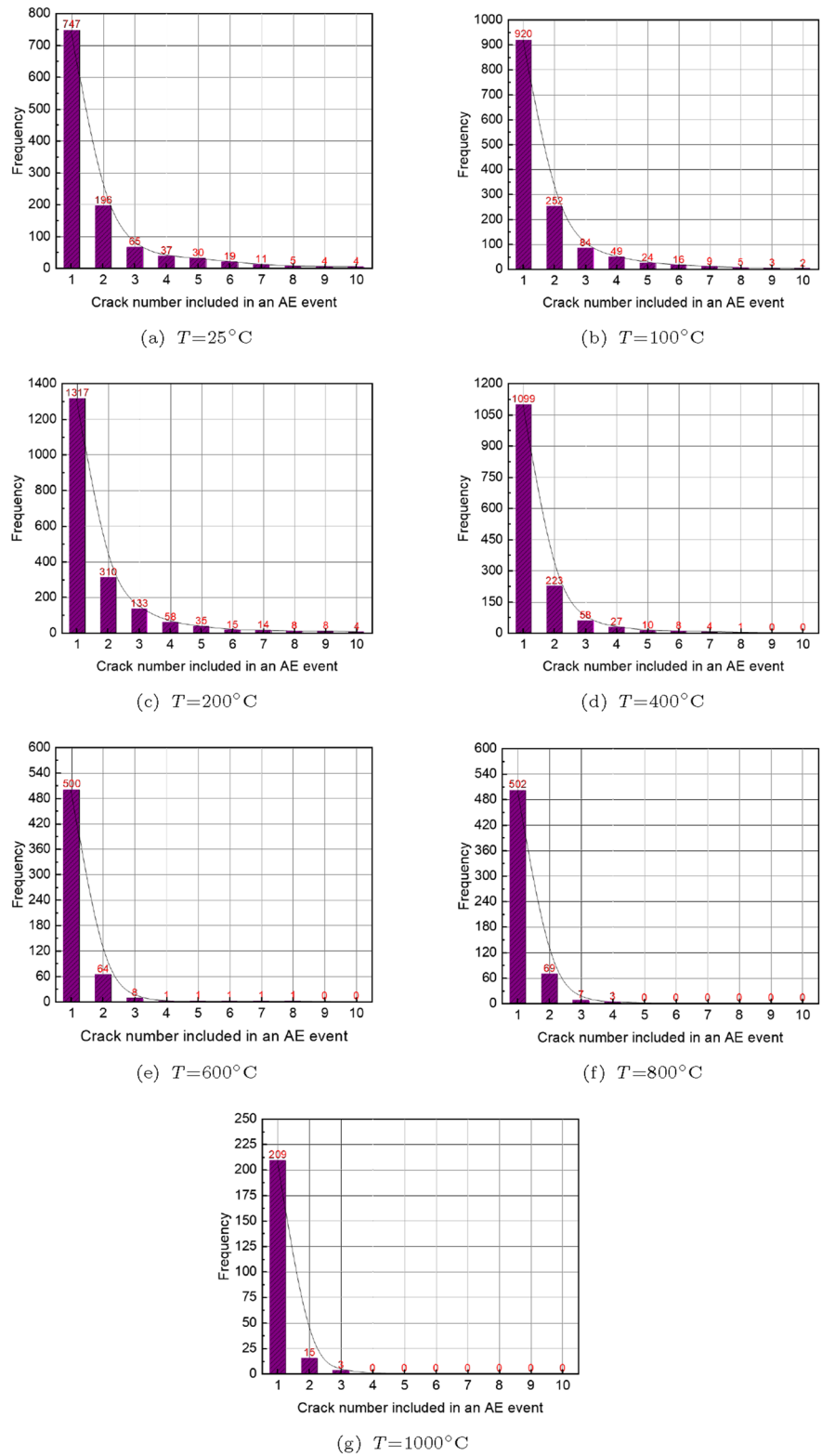
(a) $T=25°$C

(b) $T=100°$C

(c) $T=200°$C

(d) $T=400°$C

(e) $T=600°$C

(f) $T=800°$C

(g) $T=1000°$C

References

1. Becattini V, Motmans T, Zappone A et al (2017) Experimental investigation of the thermal and mechanical stability of rocks for high-temperature thermal-energy storage. Appl Energy 203:373–389

2. Gautam P, Dwivedi R, Kumar A et al (2021) Damage characteristics of Jalore granitic rocks after thermal cycling effect for nuclear waste repository. Rock Mech Rock Eng 54(1):235–254

3. Mahanta B, Ranjith P, Vishal V et al (2020) Temperature-induced deformational responses and microstructural alteration of sandstone. J Petrol Sci Eng 192(107):239

4. Orlander T, Andreassen KA, Fabricius IL (2021) Effect of temperature on stiffness of sandstones from the deep north sea basin. Rock Mech Rock Eng 54(1):255–288

5. Yu P, Pan P, Feng G et al (2020) Physico-mechanical properties of granite after cyclic thermal shock. J Rock Mech Geotech Eng 12(4):693–706

6. Jiao Y, Zhang X, Zhang H et al (2015) A coupled thermo-mechanical discontinuum model for simulating rock cracking induced by temperature stresses. Comput Geotech 67:142–149

7. Su C, Qiu J, Wu Q et al (2020) Effects of high temperature on the microstructure and mechanical behavior of hard coal. Int J Mining Sci Technol 30(5):643–650

8. Li M, Wang D, Shao Z (2020) Experimental study on changes of pore structure and mechanical properties of sandstone after high-temperature treatment using nuclear magnetic resonance. Eng Geol 275(105):739

9. Sun Q, Lü C, Cao L et al (2016) Thermal properties of sandstone after treatment at high temperature. Int J Rock Mech Mining Sci 85:60–66

10. Wu Z, Li M, Weng L (2020) Thermal-stress-aperture coupled model for analyzing the thermal failure of fractured rock mass. Int J Geomech 20(10):04020

11. Sepúlveda J, Arancibia G, Molina E et al (2020) Thermo-mechanical behavior of a granodiorite from the liquiñe fractured geothermal system (39 s) in the southern volcanic zone of the andes. Geothermics 87(101):828

12. Yang S, Huang Y, Tian W et al (2019) Effect of high temperature on deformation failure behavior of granite specimen containing a single fissure under uniaxial compression. Rock Mech Rock Eng 52(7):2087–2107

13. Rossi E, Kant MA, Madonna C et al (2018) The effects of high heating rate and high temperature on the rock strength: feasibility study of a thermally assisted drilling method. Rock Mech Rock Eng 51(9):2957–2964

14. Yin T, Shu R, Li X et al (2016) Comparison of mechanical properties in high temperature and thermal treatment granite. Trans Nonferr Metals Soc China 26(7):1926–1937

15. Jansen D, Carlson S, Young R et al (1993) Ultrasonic imaging and acoustic emission monitoring of thermally induced microcracks in lac du bonnet granite. J Geophys Res Solid Earth 98(B12):22231–22243

16. Yin T, Wu Y, Li Q et al (2020) Determination of double-k fracture toughness parameters of thermally treated granite using notched semi-circular bending specimen. Eng Fract Mech 226(106):865

17. Wong LNY, Guo TY (2019) Microcracking behavior of two semi-circular bend specimens in mode i fracture toughness test of granite. Eng Fract Mech 221(106):565

18. Nasseri M, Schubnel A, Young R (2007) Coupled evolutions of fracture toughness and elastic wave velocities at high crack density in thermally treated westerly granite. Int J Rock Mech Mining Sci 44(4):601–616

19. Jian-ping Z, He-ping X, Hong-wei Z et al (2010) Sem in situ investigation on thermal cracking behaviour of Pingdingshan sandstone at elevated temperatures. Geophys J Int 181(2):593–603

20. Wang J, Zuo J, Sun Y et al (2021) The effects of thermal treatments on the fatigue crack growth of Beishan granite: an in situ observation study. Bull Eng Geol Environ 80(2):1541–1555

21. Zhang Y, Zhao GF, Li Q (2020) Acoustic emission uncovers thermal damage evolution of rock. Int J Mech Mining Sci 132(104):388

22. Tapponnier P, Brace W (1976) Development of stress-induced microcracks in westerly granite. In: International journal of rock mechanics and mining sciences & geomechanics abstracts. Elsevier, pp 103–112

23. Rasmussen LL, de Assis AP (2018) Elastically-homogeneous lattice modelling of transversely isotropic rocks. Comput Geotech 104:96–108

24. Rasmussen LL, de Farias MM, de Assis AP (2018) Extended rigid body spring network method for the simulation of brittle rocks. Comput Geotech 99:31–41

25. Dekker R, Van der Meer F, Maljaars J et al (2019) A cohesive xfem model for simulating fatigue crack growth under mixed-mode loading and overloading. Int J Numer Methods Eng 118(10):561–577

26. Tan P, Jin Y, Pang H (2021) Hydraulic fracture vertical propagation behavior in transversely isotropic layered shale formation with transition zone using xfem-based czm method. Eng Fract Mech 248(107):707

27. Nagaraja S, Elhaddad M, Ambati M et al (2019) Phase-field modeling of brittle fracture with multi-level hp-fem and the finite cell method. Comput Mech 63(6):1283–1300

28. Goswami S, Anitescu C, Rabczuk T (2019) Adaptive phase field analysis with dual hierarchical meshes for brittle fracture. Eng Fract Mech 218(106):608

29. Rabczuk T, Belytschko T (2004) Cracking particles: a simplified meshfree method for arbitrary evolving cracks. Int J Numer Methods Eng 61(13):2316–2343

30. Ren H, Zhuang X, Cai Y et al (2016) Dual-horizon peridynamics. Int J Numer Methods Eng 108(12):1451–1476

31. Silling SA (2000) Reformulation of elasticity theory for discontinuities and long-range forces. J Mech Phys Solids 48(1):175–209

32. Zhao Z (2016) Thermal influence on mechanical properties of granite: a microcracking perspective. Rock Mech Rock Eng 49(3):747–762

33. Yang S, Tian W, Huang Y (2018) Failure mechanical behavior of pre-holed granite specimens after elevated temperature treatment by particle flow code. Geothermics 72:124–137

34. Tian W, Yang S, Huang Y et al (2020) Mechanical behavior of granite with different grain sizes after high-temperature treatment by particle flow simulation. Rock Mech Rock Eng 53(4):1791–1807

35. Yin TB, Zhuang DD, Li MJ et al (2022) Numerical simulation study on the thermal stress evolution and thermal cracking law of granite under heat conduction. Comput Geotech 148(104):813

36. Zhao X, Xu H, Zhao Z et al (2019) Thermal conductivity of thermally damaged Beishan granite under uniaxial compression. Int J Rock Mech Mining Sci 115:121–136

37. Zhao Z, Xu H, Wang J et al (2020) Auxetic behavior of Beishan granite after thermal treatment: a microcracking perspective. Eng Fract Mech 231(107):017

38. Hazzard J, Young R (2000) Simulating acoustic emissions in bonded-particle models of rock. Int J Rock Mech Mining Sci 37(5):867–872

39. Chong Z, Li X, Hou P et al (2017) Moment tensor analysis of transversely isotropic shale based on the discrete element method. Int J Mining Sci Technol 27(3):507–515

40. Zhang Q, Zhang XP, Yang SQ (2021) A numerical study of acoustic emission characteristics of sandstone specimen containing a hole-like flaw under uniaxial compression. Eng Fract Mech 242(107):430

41. Zhang Q, Zhang X, Ji P (2019) Numerical study of interaction between a hydraulic fracture and a weak plane using the bonded-particle model based on moment tensors. Comput Geotech 105:79–93

42. Wong LNY, Xiong Q (2018) A method for multiscale interpretation of fracture processes in Carrara marble specimen containing a single flaw under uniaxial compression. J Geophys Res Solid Earth 123(8):6459–6490

43. Liu Q, Liu Q, Pan Y et al (2018) Microcracking mechanism analysis of rock failure in diametral compression tests. J Mater Civil Eng 30(6):04018

44. Wanne T, Young R (2008) Bonded-particle modeling of thermally fractured granite. Int J Rock Mech Mining Sci 45(5):789–799

45. Hazzard JF, Young RP (2002) Moment tensors and micromechanical models. Tectonophysics 356(1–3):181–197

46. Heinze T, Galvan B, Miller SA (2015) A new method to estimate location and slip of simulated rock failure events. Tectonophysics 651:35–43

47. Zhao Y, Zhao G, Zhou J et al (2021) Failure mechanism analysis of rock in particle discrete element method simulation based on moment tensors. Comput Geotech 136(104):215

48. Feignier B, Young RP (1992) Moment tensor inversion of induced microseisnmic events: Evidence of non-shear failures in the- 4< m<- 2 moment magnitude range. Geophys Res Lett 19(14):1503–1506

49. Cundall PA (1971) A computer model for simulating progressive, large-scale movement in blocky rock system. In: Proceedings of the international symposium on rock mechanics, 1971

50. Cundall PA, Strack OD (1979) A discrete numerical model for granular assemblies. Geotechnique 29(1):47–65

51. Na Cho, Martin C, Sego D (2007) A clumped particle model for rock. Int J Rock Mech Mining Sci 44(7):997–1010

52. Group IC (2014) Pfc (particle flow code in 2 and 3 dimensions), version 5.0 (user's manual)

53. Li Q, Zhai Y, Huang Z et al (2022) Research on crack cracking mechanism and damage evaluation method of granite under laser action. Opt Commun 506(127):556

54. Liu S, Xu J (2015) An experimental study on the physico-mechanical properties of two post-high-temperature rocks. Eng Geol 185:63–70

55. Potyondy DO, Cundall P (2004) A bonded-particle model for rock. Int J Rock Mech Mining Sci 41(8):1329–1364

56. Ahrens TJ (1995) Mineral physics & crystallography: a handbook of physical constants, vol 2. American Geophysical Union, Washington

57. Chopard B, Droz M (2005) Cellular automata modeling of physical systems

58. Shi C, Yang W, Yang J et al (2019) Calibration of micro-scaled mechanical parameters of granite based on a bonded-particle model with 2d particle flow code. Granul Matter 21(2):1–13

59. Tian W, Yang S, Huang Y (2018) Macro and micro mechanics behavior of granite after heat treatment by cluster model in particle flow code. Acta Mech Sin 34(1):175–186

60. Zhu HY, Dang YK, Wang GR et al (2021) Near-wellbore fracture initiation and propagation induced by drilling fluid invasion during solid fluidization mining of submarine nature gas hydrate sediments. Pet Sci 18(6):1739–1752

61. Chen, S., Xia, Z., Feng, F., & Yin, D. (2021). Numerical study on strength and failure characteristics of rock samples with different hole defects. Bulletin of Engineering Geology and the Environment, 80, 1523-1540

62. Duan K, Kwok C, Ma X (2017) Dem simulations of sandstone under true triaxial compressive tests. Acta Geotech 12(3):495–510

63. Yang SQ, Ranjith P, Jing HW et al (2017) An experimental investigation on thermal damage and failure mechanical behavior of granite after exposure to different high temperature treatments. Geothermics 65:180–197

64. Huang YH, Yang SQ, Tian WL et al (2017) Physical and mechanical behavior of granite containing pre-existing holes after high temperature treatment. Arch Civil Mech Eng 17(4):912–925

65. Kong B, Wang E, Li Z et al (2016) Fracture mechanical behavior of sandstone subjected to high-temperature treatment and its acoustic emission characteristics under uniaxial compression conditions. Rock Mech Rock Eng 49(12):4911–4918

66. Tian H, Mei G, Jiang GS et al (2017) High-temperature influence on mechanical properties of diorite. Rock Mech Rock Eng 50(6):1661–1666

67. Gao G, Meguid MA, Chouinard LE (2020) On the role of pre-existing discontinuities on the micromechanical behavior of confined rock samples: a numerical study. Acta Geotech 15(12):3483–3510

68. Grosse CU, Ohtsu M (2008) Acoustic emission testing. Springer, London

69. Falls SD (1995) Ultrasonic imaging and acoustic emission studies of microcrack development in lac du bonnet granite. PhD thesis, Queen's University

70. Hazzard, James F (1998) Numerical modelling of acoustic emissions and dynamic rock behaviour. PhD thesis, University of Keele